



LAWRENCE
LIVERMORE
NATIONAL
LABORATORY

X-ray Induced Pinhole Closure in Point Projection X-ray Radiography

A.B. Bullock, O.L. Landen, B.E. Blue, J. Edwards,
D.K. Bradley

January 25, 2006

Journal of Applied Physics

Disclaimer

This document was prepared as an account of work sponsored by an agency of the United States Government. Neither the United States Government nor the University of California nor any of their employees, makes any warranty, express or implied, or assumes any legal liability or responsibility for the accuracy, completeness, or usefulness of any information, apparatus, product, or process disclosed, or represents that its use would not infringe privately owned rights. Reference herein to any specific commercial product, process, or service by trade name, trademark, manufacturer, or otherwise, does not necessarily constitute or imply its endorsement, recommendation, or favoring by the United States Government or the University of California. The views and opinions of authors expressed herein do not necessarily state or reflect those of the United States Government or the University of California, and shall not be used for advertising or product endorsement purposes.

X-Ray Induced Pinhole Closure in Point Projection X-ray Radiography*

A.B. Bullock, O.L. Landen, B.E. Blue, J. Edwards, and D.K. Bradley

Lawrence Livermore National Laboratory, Livermore CA 94550

Abstract

In pinhole-assisted point-projection x-ray radiography (or "backlighting"), pinholes are placed between the sample of interest and an x-ray source (or "backlighter") to effectively limit the source size and hence improve the spatial resolution of the system. Pinholes are generally placed close to such x-ray backlighters to increase the field-of-view, leading to possible vaporization and pinhole closure due to x-ray driven ablation, thereby potentially limiting the usefulness of this method. An experimental study and modeling of time-dependent closure and resolution is presented. The pinhole closure timescale is studied for various pinhole sizes, pinhole to backlighter separations and filtering conditions. In addition the time-dependent resolution is extracted from one-dimensional wire imaging prior to pinhole closure. Cylindrical hydrodynamic modeling of the pinhole closure shows reasonable agreement with data, giving us a predictive capability for pinhole closure in future experiments.

*This work was performed under the auspices of the U.S. Department of Energy by the University of California Lawrence Livermore National Laboratory under Contract W-7405-ENG-48.

I. Introduction

Radiographic imaging of high-density samples using x-ray backlighting is an important diagnostic technique in high energy density experiments that have been performed on the Nova¹, OMEGA² and NIF³ laser facilities. Experiments involving both laser-driven⁴⁻⁶ and x-ray driven⁷⁻¹⁰ samples have used x-ray backlighting to probe physical details in high density samples too opaque to allow optical probing. Many of these experiments use laser-driven foils to produce the imaging x-rays, and these x-rays image the experimental sample in several experimental geometries.¹¹

A specific geometry, pinhole-assisted point-projection backlighting (see Figure 1), is especially useful and important for the large samples sizes encountered on NIF¹⁰⁻¹⁴. This method allows imaging of large targets without requiring a prohibitively large backlighter plasma size s and hence laser power, with the resolution still set by the pinhole diameter D for as long as it remains open. However, the combination of large samples and a maximum distance $d + p$ between backlighter and driven sample as set by beam pointing travel limits requires the pinhole be placed small distances d (of order 1 mm) away from the backlighter to maintain a large imaging solid angle $\sim (s/d)^2$. To motivate the subsequent experimental and hydrodynamic modeling work to be presented, we first consider simple analytic estimates of x-ray ablation effects from such a close proximity backlighter source to a pinhole.

For a typical backlighter laser power of 1 TW converted with 0.1% efficiency to isotropically emitted backlighter x-rays, the pinhole substrate front surface and walls can receive incident x-ray intensities of order $I = 10 \text{ GW/cm}^2$ at 1 mm. It is then instructive

to equate the absorbed energy density $I_{\max}\tau/\text{mfp}$ to the heat capacity of $10^4 \text{ J/cm}^2/\text{eV/atom}$ for a typical high Z pinhole substrate such as Ta. For a typical Ti resonance line backlighter photon energy of 4.75 keV with mean free path (mfp) = 1 μm in Ta, $I_{\max} = 10 \text{ GW/cm}^2$ leads to an energy deposition rate/atom of $\approx 10 \text{ eV/ns}$. Hence we would expect a few eV plasma formed over a thickness = $\text{mfp}\sin\theta$ at the inner Ta walls within 1-2 ns, where θ is the average angle from grazing incidence subtended by the source at the walls, typically 0.2 radians. Ignoring for the moment heat conduction losses inward, such a plasma would then blow-off at the isothermal plasma sound speed $c_s = \sqrt{(ZT_e/m_i)}$, of order 1.5 $\mu\text{m/ns}$ for a singly ionized $T_e = 3 \text{ eV}$ plasma. Substantial absorption is to be expected when the blow off plasma density exceeds a threshold density defined by the ratio of the solid density mfp to the pinhole length. For a typical 50 μm long pinhole in a Ta substrate, this threshold density is $\approx 0.3 \text{ g/cc}$ (1/50th of solid Ta density). In the self-similar isothermal expansion model¹⁵, this threshold density contour will blow-off at a velocity of $c_s[\ln(50) - 1] \approx \text{Mach } 3, \approx 4 \mu\text{m/ns}$. Moreover, the areal density of heated wall material = $15 \text{ g/cc} \times \text{mfp}\sin\theta = 0.3 \text{ mg/cm}^2$ is sufficient to support filling at 0.3 g/cc over the full pinhole radius. Hence, ablation should occur and enough ablated material is available quickly enough to fill the pinhole with opaque material on the ns timescale, thereby blocking the x-rays and eventually ‘closing’ the pinhole. Given up to 3x variations in x-ray conversion efficiencies reported previously^{16,17} and inherent complexities of modeling non-ideal low temperature dense plasmas¹⁸, it is hence important to measure the onset of closure in current experiments and use the results to validate hydrodynamic computations that could serve as a predictive tool for future experiments.

Using 10 μm and 5 μm pinholes¹² and slits, we have hence studied and modeled pinhole and slit closure in pinhole-assisted point-projection imaging using a 4.7 keV Ti backlighter. Streaked backlit images of W wires are analyzed to infer time-dependent pinhole and slit transmission and size for various filtration conditions and various values of d and D . The results are first compared with a simple model of pinhole transmission based on an infinitely ‘steep’ ablated converging material density front. The HYADES¹⁹ hydrodynamics code is then used for more accurate modelling of x-ray driven pinhole closure, using physically-reasonable assumptions regarding laser-to-x-ray conversion efficiency, and the Ta pinhole substrate equation of state.

II. Experimental Set-Up

Ablation and closure of 5 μm and 10 μm pinholes during point-projection backlit imaging was studied¹⁰ with targets consisting of a 12.7 μm thick Ti backlighter foil, a ‘primary’ pinhole, 10 μm or 5 $\mu\text{m} \pm 0.5 \mu\text{m}$ in diameter, and a ‘reference’ pinhole, $23 \pm 1 \mu\text{m}$ in diameter (see Figure 2). Both pinholes have been laser cut in 50 μm -thick Ta and view the backlighter foil at 45° to its normal from opposite sides. The ‘primary’ pinhole is positioned at a distance $d = 0.45$ or 1 mm from the backlighter foil for which pinhole ablation and closure are expected within a 1-3 ns timescale. The larger ‘reference’ pinhole is positioned at a greater distance $d = 1.5 \text{ mm}$ from the backlighter and is not expected to close. This allows monitoring of the backlighter intensity by monitoring the x-ray emission through this ‘reference’ pinhole. A set of three 25 μm W wires placed at $p = 1.5 \text{ mm}$ away from both the ‘primary’ and ‘reference’ pinhole serve as test objects to

determine system resolution. Wire-to-wire separation in each set is approximately 100 μm , and this value is measured accurately before each shot so as to provide a system magnification after the shot. An x-ray streak camera is placed 15 cm behind each pinhole to record the signal strength and resolution of the backlit x-ray images of the wires as a function of time.

During the experiment, the backlighter front surface is illuminated with six 3ns, 351 nm laser pulses from the Omega Laser incident at 20-25° to the foil normal. The laser spot size at the foil is 250 μm and the total beam power P_L on target is 0.6 TW, providing an intensity of 10^{15} W/cm². The He-like n=2-1 resonance line x-rays emitted at 4.75 keV from the resulting plasma propagate through the Ti essentially minimally attenuated. The solid cone of x-rays that propagates through each pinhole backlights the W wire set. The wires are imaged at ~100x magnification onto the photocathode slit of the streak camera, producing a swept (120ps/mm) 1-D image of the W wire shadow. The resulting film image then shows the time history (30 ps resolution) of the 1-D wire shadow produced with the pinhole.

The Ti backlighter and each pinhole combine to function as a quasi-point source of x-rays. Streaked images of the wire shadow have a spatial resolution that is only weakly dependent on the resolution σ_{SC} of the streak camera itself ($\sigma_{SC}/M \approx 1 \mu\text{m}$) and mainly determined by the finite dimensions of the x-ray pinhole. The latter dependence is given by the expression²⁰,

$$\sigma^2 = \left(\frac{M+1}{M} D\right)^2 + \left(2.44 \lambda \frac{P}{D}\right)^2 \quad (1)$$

where D is the pinhole diameter, M is the magnification, p is the distance from the pinhole to wires, and λ is the characteristic wavelength. For our experiment, p is 1.5 mm, $D \geq 5 \mu\text{m}$, and $\lambda = 0.26 \text{ nm}$. This results in negligible diffraction (second term in Eq. (1), $< 0.2 \mu\text{m}$) relative to the finite size of the pinhole (first term = 5 – 10 μm) that dominates the resolution.

III. Experimental Results

Figure 3 shows streaked images produced by the ‘primary’ 10 μm pinhole (A) and the ‘reference’ 23 μm pinhole (B). Here, the 10 μm pinhole was placed 0.45 mm away from the backlighter. The wire shadow produced by the 23 μm pinhole is visible at 2ns, which implies that the 23 μm pinhole does not ablate and close appreciably on this timescale. The wire shadow produced with the 10 μm pinhole is clearly visible after 500 ps, but starts to disappear at 1 ns. The time-dependent intensity of the x-rays propagating through the 10 μm pinhole is measured from the streaked image in the region adjacent to the wire shadow. The time-dependent intensity of the x-rays propagating through the 23 μm pinhole is also measured, and this intensity is assumed to correspond to the relative backlighter source intensity. By normalizing the x-ray intensity from the 10 μm pinhole to the 23 μm pinhole data, a plot of 10 μm pinhole transmission is produced (see Figure 4). The plot shows that the pinhole transmission value is approximately unity until 500ps after the start of the backlighter. At that point, the transmission drops sharply to 50% transmission at 0.8 ns and to zero at 1.3 ns. This delayed closure followed by a rapid drop in transmission is consistent with a threshold Ta surface temperature that must be

exceeded before appreciable ablation can occur. Point-projection backlit imaging using 10 μm pinholes at 0.45 mm from this 0.6 TW backlighter is therefore limited to times less than 0.8 ns. Figure 4 also shows transmission for a 10 μm pinhole placed 1 mm away from the backlighter. In this case, transmission stays constant until approximately 900 ps after start of the backlighter, suggesting that the temperature of the pinhole wall surface increases more slowly as expected for a more distant pinhole. The pinhole closure timescale is also longer, dropping to 50% in 1.5 ns and to zero soon after 2 ns. Similarly, Figure 5 compares the time-dependent transmission of a 5 μm and 10 μm pinhole placed 1 mm away from the backlighter. The 5 μm pinhole begins to close 200 ps after start of the backlighter, reaches 50% transmission at 0.4 ns, and full closure at 0.6 ns. The timescale for the pinhole transmission to drop to 50% is 0.5 ns.

For providing a predictive modelling capability scaling to full NIF, a more complete picture of the ablation dynamics can be inferred by also considering the time-dependent resolution provided by the closing pinhole. These dynamics are studied by measuring the resolution of 1-D W wire shadow images produced by the pinhole. Figure 6b shows a plot of the 1-D wire shadow image produced by a 10 μm pinhole placed 0.45mm away from the backlighter. This plot was produced by averaging over the temporal range 460 to 700 ps. Also shown is a fit to the wire shadow calculated by convoluting an infinitely sharp model of the wire shadow with the line spread function of a 10.6 μm round pinhole. Similarly, wire shadows produced by 5 μm and 23 μm pinholes are shown with calculated wire shadows in Figures 6a and c, respectively. We get a best fit of the experimental wire shadow image by calculating the χ^2 goodness-of-fit between the experimental wire shadow and the modeled wire shadow as the diameter of

an assumed round pinhole is varied. The best-fit diameter as a function of time is plotted in Figure 7 for the 10.6 μm pinhole images.

In the case of a steep, ‘hard aperture’ density profile, the effective diameter D' of the pinhole is expressed as $D' = DT^{0.5}$, where T is the measured transmission and D is the initial diameter of the pinhole prior to the experiment. A plot of the expected pinhole diameter using this simple model is also shown on Figure 7. Clearly, the measured pinhole diameter does not agree with the expected pinhole diameter. This indicates that the center regions of the pinhole (diameters $< D'$) fill up to a sufficient Ta atomic density such that transmission through the center region is also substantially attenuated, and that a simple hard aperture closing model is inadequate.

IV. Hydrodynamic Modeling

To further understand the dynamics of pinhole closure, we used the one-dimensional, Lagrangian hydrodynamics and energy transport code HYADES to model pinhole transmission. We model pinhole transmission by using HYADES to simulate the x-ray driven ablation of a small region of the pinhole wall (δA) in cylindrical geometry (see Figure 8a). HYADES includes the effects of conduction into the Ta as well as expansion into the pinhole. HYADES calculates the ablated Ta atomic density as a function of time and radius from the center of the pinhole (see Figure 8(b)). Using the cold opacity of Ta atoms valid for photon energies \gg plasma temperature, we then calculate the 4.7 keV x-ray transmission $\delta T(r,t)$ through a small longitudinal depth through the pinhole, δL . We initially assume that the x-ray fluence is independent of

longitudinal position inside the pinhole (valid since the pinhole length of 50 μm is $\ll d$), and by integrating $\delta T(r,t)$ over the full length of the pinhole, we calculate x-ray transmission through the full pinhole, $T(r,t)$. We then spatially average $T(r,t)$ over the pinhole cross-sectional area to solve for total pinhole transmission.

The HYADES simulation of Ta pinhole inner wall ablation starts with energy deposited volumetrically into a small depth of Ta (see Fig. 8c). Since the depth of the heated Ta volume is determined by the average angle of incidence of the 1 μm mfp 4.7 keV backlighter x-rays arriving at the Ta surface, this depth varies with the distance between the backlighter and the pinhole (0.2 μm for a distance of 0.45 mm, 0.1 μm for a distance of 1 mm). The x-ray drive is treated as monochromatic since the Ti foil self-filtering extinguishes Ti x-ray lines with photon energy above that of the Ti K edge (5.0 keV) and soft x-ray framing camera images of the Ti backlighter show that negligible soft x-ray fluence ($F_{\text{soft}}/F_{4.7 \text{ keV}} < 0.001$) should arrive at the pinhole. Soft x-ray ablation could be more efficient at small pinhole closure since their mfp in Ta is much shorter, leading to greater heating and greater blow-off velocity. Hence, a direct test of the importance of any ablation due to soft x-rays emitted by the heating of the backside of the Ti foil was performed. Figure 9 shows the measured pinhole closure with and without 125 μm of Be placed between the Ti foil and pinhole. The Be would have absorbed any soft x-rays below 2 keV while transmitting 90% of the Ti He- α 4.75 keV x-rays. The similarity in closure dynamics is further proof that soft x-rays are not responsible for closure in this case. For pinhole-side illuminated foils¹⁴, soft x-rays from the hot laser plasma could cause pinhole closure and low Z shielding is recommended.

Since the absolute laser-to-x-ray conversion efficiency is not well known, we used an assumed value for the conversion efficiency that we vary as an adjustable parameter to maximize fit between the data and the model. We used the in-line quotidian equation of state in the HYADES simulation, with an assumed bulk modulus of $2 \times 10^5 \text{ J/cm}^3$. We also used the Thomas-Fermi ionization model for the simulation. Fig. 10 shows the HYADES calculations of the temperature and density profile in a $10 \mu\text{m}$ pinhole at 1 mm to the backlighter at the 50% transmission time. We note the increased temperature at pinhole center attributed to convergent plasma stagnation.

Figure 11 shows the HYADES-calculated transmission for $10 \mu\text{m}$ pinholes placed both 0.45 mm and 1 mm away from the Ti backlighter. The actual x-ray drive temporal profile was used in the modelling for each case. The laser to x-ray energy conversion efficiency was the one adjustable parameter. We have best fit the data on Figure 11 by assuming 0.1% of the laser energy is converted into isotropically emitted 4-10 keV x-rays. This is consistent with the range of previous Ti conversion efficiency data¹⁵ at 3ω when folding in the 50% transmission²¹ of the Ti foil at 45° . X-ray fluence and flux I is expected to scale as $1/d^2$, recalling that d is the distance between the backlighter and the pinhole. We note that the closure time ($\sim 1/\text{sound speed } c_s$) predicted by HYADES on Fig. 11 scales close to $d^{2/3}$ as would be expected if we equate the incident x-ray intensity $I \sim 1/d^2$ to plasma flux $\sim \rho c_s^3$. Similarly, a 30% change in assumed x-ray conversion efficiency changes the 50% closure time by $\approx 10\%$. The model, while predicting the 1 mm case closure time, overpredicts the effects of closure for the 0.45 mm case probably because of vignetting effects in these moderate (5-10) aspect ratio pinholes. Specifically, by simple geometry, we expect the 5x aspect ratio of the $10 \mu\text{m}$ pinhole prevented the

deeper regions inside the pinhole from seeing the full 0.25 mm backlighter plasma size at the shorter distance of 0.45 mm. This would reduce the total ablated areal density traversed by the imaging x-rays, which would explain the fact that the 0.45 mm data shows a slower pinhole closure than the 1D model. We have not attempted to further model this vignetting as its effects would depend strongly on the exact cross-sectional shape of the pinhole with depth that was not characterized. For example, for a conical rather than cylindrical thick pinhole shape, we would expect less (more) ablation with the thin (thick) end pointed towards the backlighter plasma. HYADES also shows that negligible ablation occurs until the Ta temperature exceeds a threshold ablation temperature of 0.5 eV. This agrees with experimental observations mentioned previously, and this agreement suggests the chosen equation of state is reasonable.

Figure 12 compares measurements and HYADES calculations of pinhole size during ablation and closure in which the 10.6 μm pinhole-to-backlighter distance is 0.45 mm. Here, the HYADES calculated pinhole size is calculated by measuring the radial position at which the transmission, $T(r,t)$, drops to 1%. Choosing a different transmission point (e.g. 3%) would not significantly change the perceived resolution. This defines the maximum effective pinhole diameter and therefore pinhole size. There is much better agreement than with the simple hard aperture model. In particular, the pinhole diameter does not decrease more than 20% in both the HYADES simulations and data in the first 1 ns.

5 and 10 μm slit closure data (Fig. 13) was also recorded. Such slits could be used for 1D gated or streaked radiography, or for 2D radiography using two crossed slits. We note that the final closure for the 10 μm slit occurs later (at 1.7 ns) than for the 10 μm

pinhole (at 1.2 ns), consistent with the larger (2x greater) open volume-to-surface area provided by a slit.

V. Summary

We have studied the pinhole closure dynamics of 5 μm and 10 μm pinholes subject to intense x-ray fluxes from nearby laser plasma sources. We have measured the transmission of 5 μm pinholes positioned 1.0 mm away from a Ti backlighter and found the timescale for 50% pinhole closure to be as short as 400 ps. The transmission of 10 μm pinholes positioned both 0.45 mm and 1.0 mm away from the backlighter was also measured, and the timescales for 50% closure were 0.9 ns and 1.4 ns, respectively. All these times are sufficient for providing adequate photon collection for radiography experiments. Moreover, one could envisage using the pinhole closure as a feature for providing automatic gating of images recorded by simple static detectors such as x-ray film or CCDs. The effective diameter of the 10 μm pinhole, measured by analysis of the 1-D wire shadow resolution, did not change significantly in time. This suggests that pinhole transmission losses were in part due to partial transmission in regions near the center of the pinhole. Moreover, the source of the closure was demonstrated to be due to multi-keV x-rays, and not due to softer x-rays which are mitigated by irradiating the backlighter foil from the backside. HYADES modeling confirmed these results and demonstrates reasonable agreement between the modeling and the data for an assumed physically plausible laser-to-x-ray conversion efficiency of 0.1%.

We expect timescales for pinhole closure to scale as the x-ray flux at the pinhole $\sim \eta P_L/d^2$, where η is the conversion efficiency. For the NIF single beam (single quad of beams) experiments^{6,22} with power 4(16)x greater than current experiments at Omega (2.4(9.6) TW vs 0.6 TW), the pinhole stand-off distance d for fixed η and closure time should hence be made 2(4)x greater, 2 - 4 mm. Moreover, even the minimum spot size of 0.3 mm on NIF should provide an acceptable sample field-of-view of $sp/d = 3$ mm for a typical value of $p = 3$ cm, providing minimal parallax from one edge of the image to the other.

We note that current experiments plan to extend the technique of pinhole or slit-assisted point projection backlighting to 1D streaked absorption or refraction enhanced^{6,23,24} radiography over several ns, which require further efforts at delaying pinhole or slit closure, for example by tamping of pinholes with low Z x-ray transparent materials. To be confident that pinholes have been fully filled with low Z tamper material throughout their length before testing the efficacy of tamping, one could instead coat Ta edges with thin Be or plastic, and join together to form a tamped slit. A pinhole could then be constructed by using two crossed slits²⁵. Such tests with tamped pinholes should be the focus of future research, especially for new schemes using front illuminated (i.e. pinhole-side illuminated) backlighter disks¹⁴, which subject the pinhole substrate to higher spectrally integrated x-ray fluences.

Acknowledgements

The authors would like to thank the staff at OMEGA for their expert operations and technical advice. We also thank R. Costa, S. Alvarez, K. Loughman, T. James, R.

Wallace, M. Spragge, R. Barksdale, V. Rekow, J. Ruppe, D. Mathews, and C. Rivers for their outstanding technical assistance. We would like to thank Jon Larsen of Cascade Applied Sciences for his expert advice on the HYADES code. We also want to thank W. Hsing for his continuing support.

References

1. J.D. Kilkenny, Phys. Fluids **6**, 1400 (1990).
2. T.R. Boehly, D.L. Brown, R.S. Craxton, R.L. Keck, *et. al.*, Opt. Comm. **133**, 495 (1997).
3. G.H. Miller, E.I. Moses and C.R. Wuest, Nucl. Fusion **44**, 228 (2004).
4. B. Yaakobi, D. Shvarts, R. Epstein, and Q. Su, Laser Part. Beams **14**, 81 (1996).
5. V.A. Smalyuk, T.R. Boehly, D.K. Bradley, V.N. Goncharov, *et. al.*, Phys. Rev. Lett. **81**, 5342 (1998).
6. B.E. Blue, *et. al.*, Phys. Rev. Lett. **94**, 095005 (2005); B.E. Blue, *et. al.*, Phys. Plasmas **12**, 056313 (2005).
7. S. G. Glendinning, P. Amendt, B.D. Cline, R.B. Ehrlich, *et. al.*, Rev. Sci. Instrum. **70**, 536 (1999).
8. D.H. Kalantar, S.W. Haan, B.A. Hammel, C.J. Keane, O.L. Landen, and D.H. Munro, Rev. Sci. Instrum. **68**, 814 (1997).
9. W.W. Hsing and N.M. Hoffman, Phys. Rev. Lett. **78**, 3876 (1997).
10. D.K. Bradley, O.L. Landen, A.B. Bullock, S.G. Glendinning and R.E. Turner, Opt. Lett. **27**, 134 (2002).
11. O.L. Landen, D.R. Farley, S.G. Glendinning, L.M. Logory, *et. al.*, Rev. Sci. Instrum., **72**, 627 (2001).
12. A.B. Bullock, O.L. Landen and D.K. Bradley, Rev. Sci. Instrum. **72**, 690 (2001).
13. J. Workman, J.R. Fincke, P. Keiter, *et. al.*, to be published in Rev. Sci. Instrum.
14. B. Blue, J.F. Hansen, and H.F. Robey, Rev. Sci. Instrum. **75**, 3989 (2004).

15. W.L. Kruer, "Physics of Laser Plasma Interactions", (Addison-Wesley, Redwood City, 1988).
16. R.L. Kauffman, "Physics of Laser Plasma", Eds. A. Rubenchik and S. Witkowski, (North-Holland, Amsterdam, 1991) pp. 116-117.
17. D.L. Matthews, E.M. Campbell, N.M. Ceglio, G. Hermes, *et. al.*, J. Appl. Phys. **54**, 4260 (1983).
18. Y.T.. Lee and R.M. More, Phys. Fluids **27**, 1273 (1984).
19. J. Larsen and S.M. Lane, J. Quant. Spectrosc Radiat Trans. **51**, 179 (1994).
20. J.A. Koch, O.L. Landen, T.W. Barbee, Jr., P. Celliers, *et. al.*, Appl. Opt. **37**, 1784 (1998).
21. A.B. Bullock, O.L. Landen and D.K. Bradley, Rev. Sci. Instrum. **72**, 686 (2001).
22. S.H. Glenzer, *et. al.*, Nucl. Fusion **44**, S185 (2004).
23. B. J. Kozioziemski, J.D. Sater, J.D. Moody, *et. al.*, J. Appl. Phys. **98**, 103105 (2005).
24. D.S. Montgomery, A. Nobile, and P.J. Walsh, Rev. Sci. Instrum. **75**, 3986 (2004).
25. O.L. Landen, P.M. Bell, R. Costa, D.H. Kalantar, and D.K. Bradley, SPIE, Vol. **2549**, 38 (1995).

Figure Captions

Figure 1. Diagram of pinhole-assisted point projection backlighter geometry.

Figure 2. Diagram of the experimental target. The backlighter foil, the ‘primary’ pinhole, and the ‘secondary’ pinhole are all mounted on edge to a 100 μm polycarbonate base (not shown). The W wire sets are shown as a set of three dots in the diagram.

Figure 3. Time-streaked images of a 25 μm W shadow produced with the 10 μm diameter ‘primary’ pinhole (A) and the 23 μm diameter ‘reference’ pinhole (B). Time is shown vertically, and lighter pixel shade indicates higher x-ray fluence. Here, the 10 μm pinhole was placed 0.45 mm away from the backlighter, and the 23 μm pinhole was placed 1.5 mm away from the pinhole.

Figure 4. 10 μm pinhole transmission for pinhole-to-backlighter distances of both 0.45 mm (open squares) and 1 mm (closed circles).

Figure 5. 5 μm (open circles) and 10 μm (closed squares) pinhole transmission for pinholes placed 1 mm away from the backlighter.

Figure 6. Measured lineout and fitted resolution for 5, 10 and 23 μm pinhole images of 25 μm W wire. Data separated along y-axis. Top data taken at $t = 150$ ps by a 5 μm pinhole placed 1 mm away from the backlighter is best fit using a 5.1 μm pinhole

resolution. Middle data taken at $t = 600$ ps by a $10\ \mu\text{m}$ pinhole placed 0.45 mm away from the backlighter is best fit using a $10.6\ \mu\text{m}$ pinhole resolution. Bottom data taken at $t = 600$ ps by a $23\ \mu\text{m}$ pinhole 1.5 mm away is best fit using a $23.5\ \mu\text{m}$ pinhole resolution.

Figure 7. $10\ \mu\text{m}$ pinhole transmission (closed circles) and resolution (open squares) for pinhole-to-backlighter distances of 0.45 mm. Solid line is calculated resolution assuming pinhole closes as hard aperture based on measured transmissions.

Figure 8. Diagram of pinhole closure geometry for HYADES simulations. a) X-ray driven pinhole ablation is simulated in a small region, dA . b) The simulation calculates density as a function of distance from the surface in a cylindrical geometry, which is equivalent to density as a function of radius. c) The depth of x-ray heating is controlled by the mean free path of 4.7 keV x-rays in Ta and the average angle of incidence for the x-rays.

Figure 9. Transmission of $10\text{-}\mu\text{m}$ pinhole at 0.45 mm to backlighter, with (open circles) and without (closed squares) $125\ \mu\text{m}$ Be between Ti and pinhole.

Figure 10. Plot of HYADES-calculated Ta density (dashed line) and ion temperature (solid line) as a function of radius inside $10\ \mu\text{m}$ pinhole at the time at which the spatially-averaged pinhole transmission is 50%.

Figure 11. Measured (symbols) and corrected, hard x-ray only HYADES simulation (curves) of transmission for 10 μm pinhole at 0.45 mm (open circles and solid line) and 1 mm (closed squares and dashed line) from 0.5 TW Ti backlighter.

Figure 12. Measured (symbols) and corrected, hard x-ray only HYADES simulation (curves) of transmission and resolution for 10- μm pinhole at 0.45 mm from 0.5 TW Ti backlighter.

Figure 13. 5 μm (open circles) and 10 μm (closed circles) slit transmission for slits placed 0.45 mm away from the backlighter.

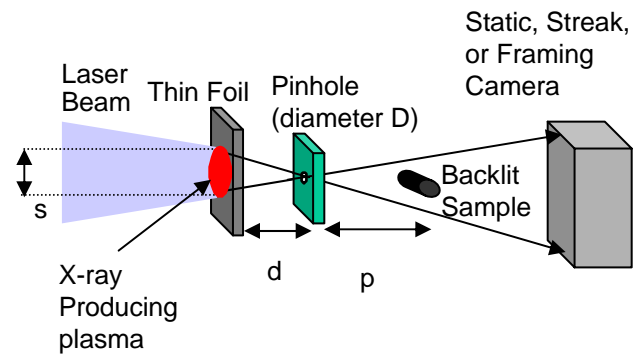


Figure 1

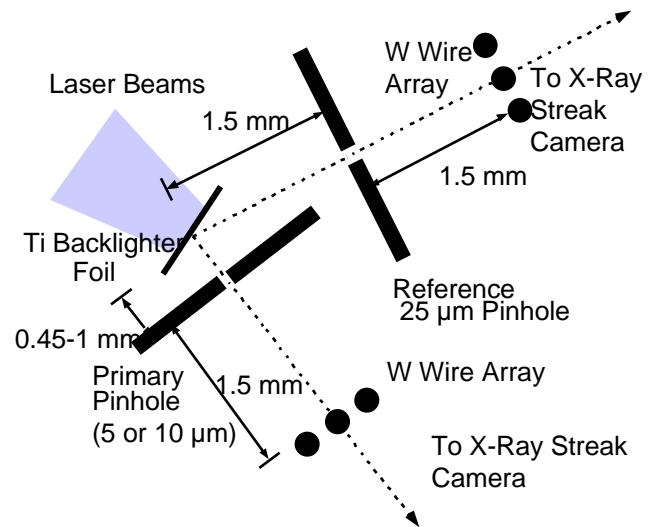


Figure 2

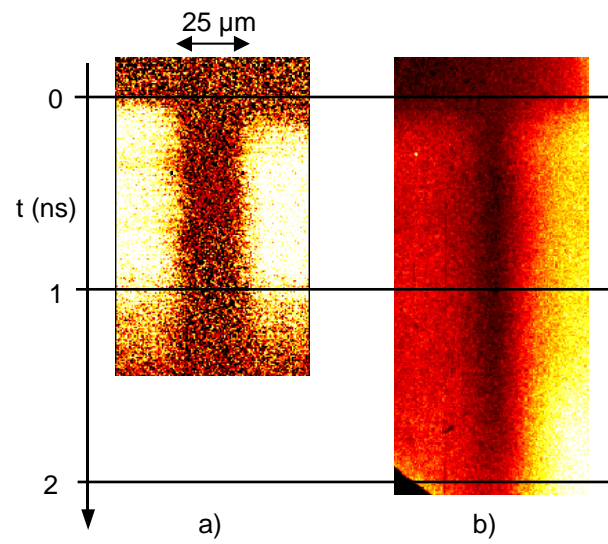


Figure 3

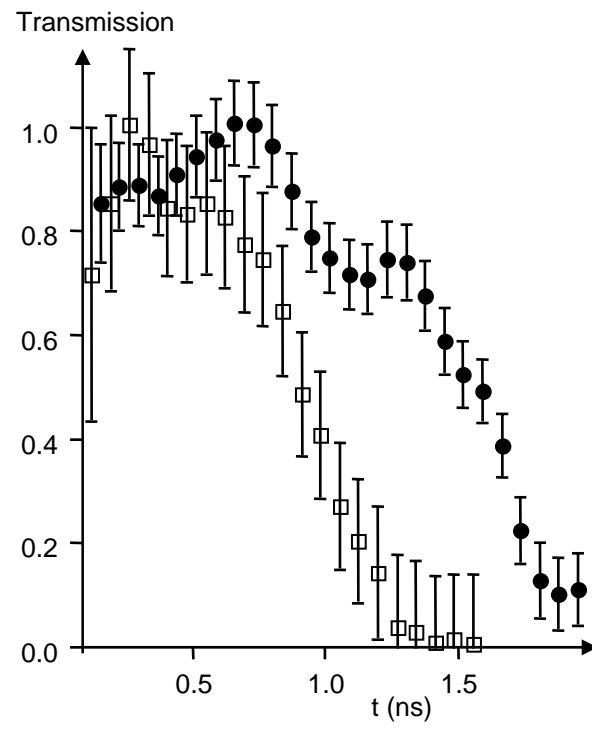


Figure 4

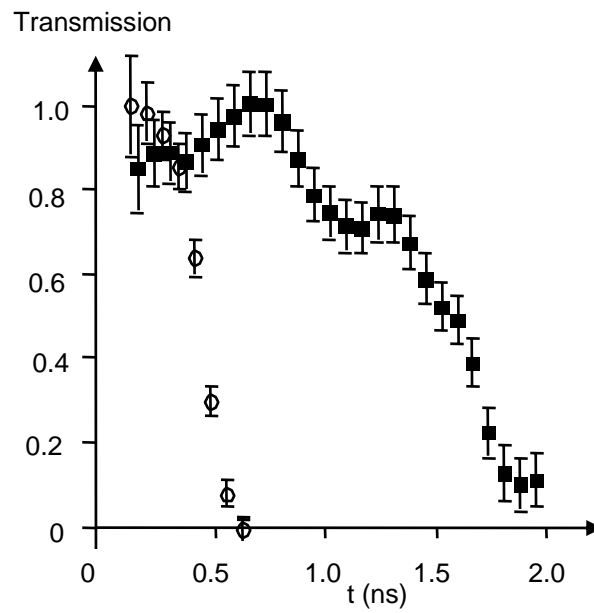


Figure 5

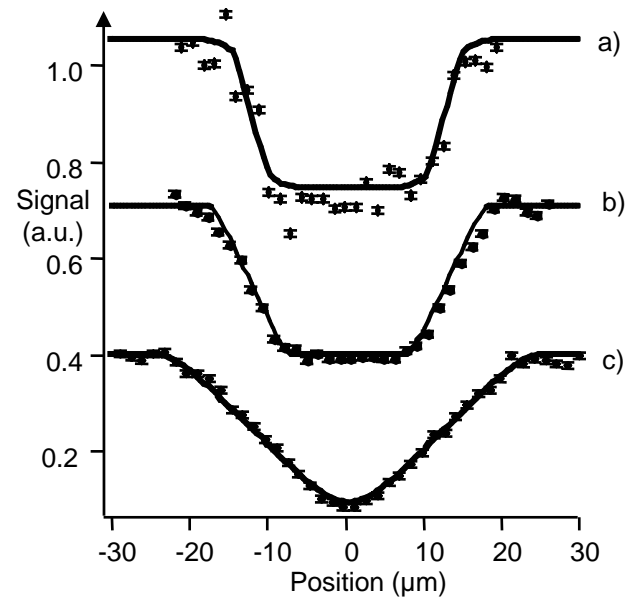


Figure 6

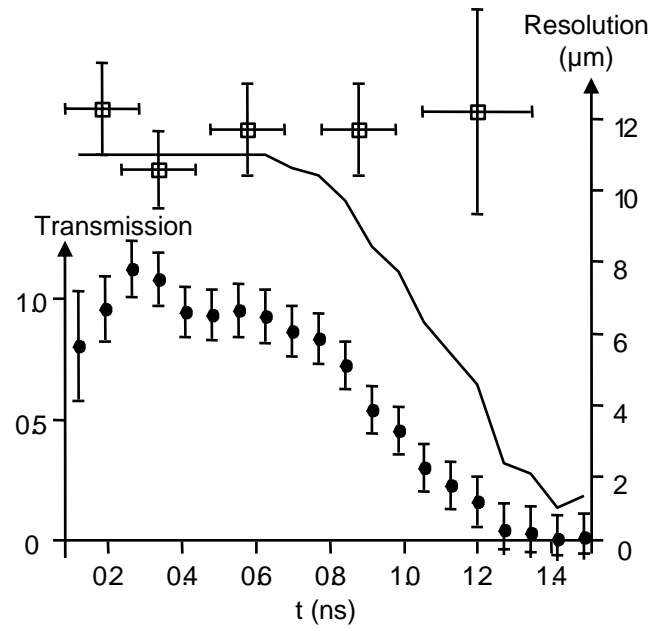


Figure 7

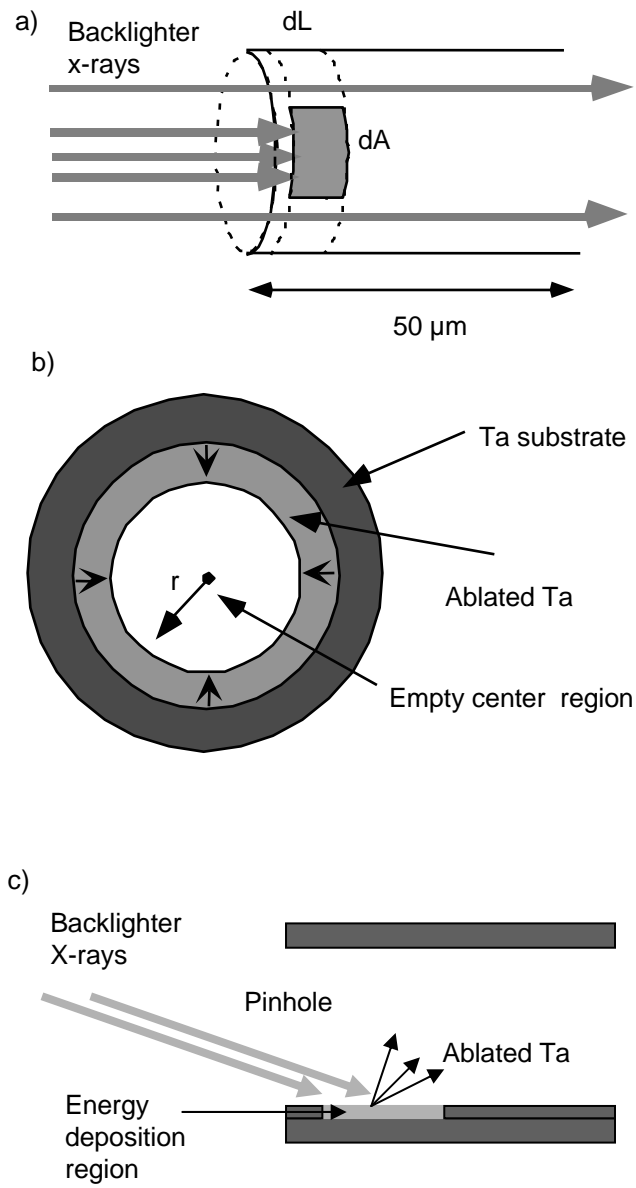


Figure 8

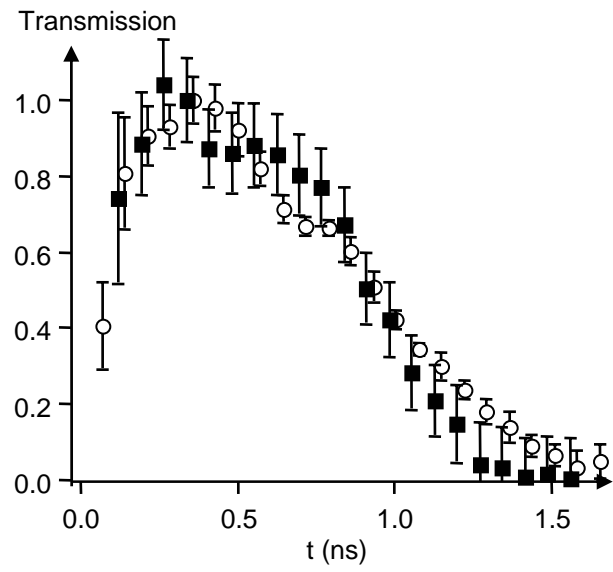


Figure 9

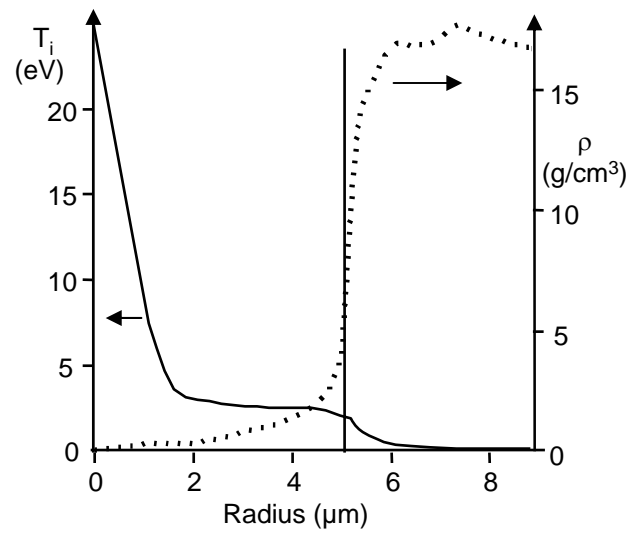


Figure 10

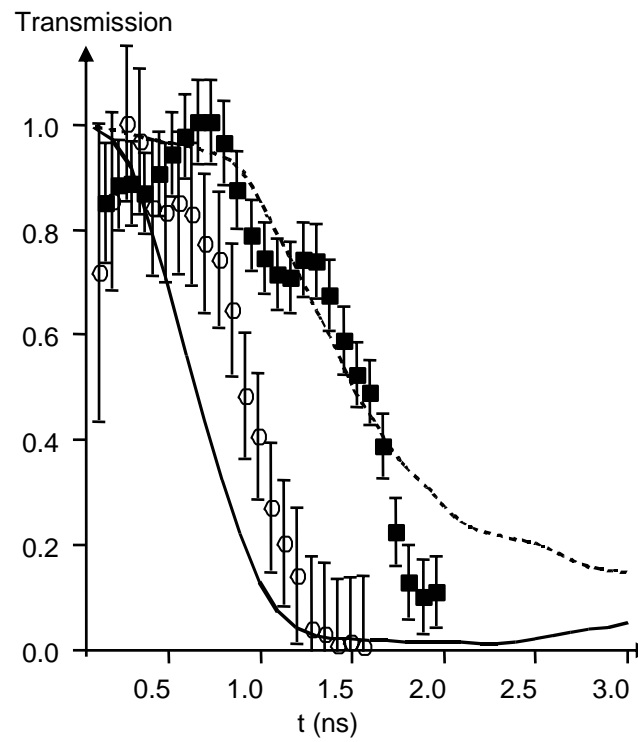


Figure 11

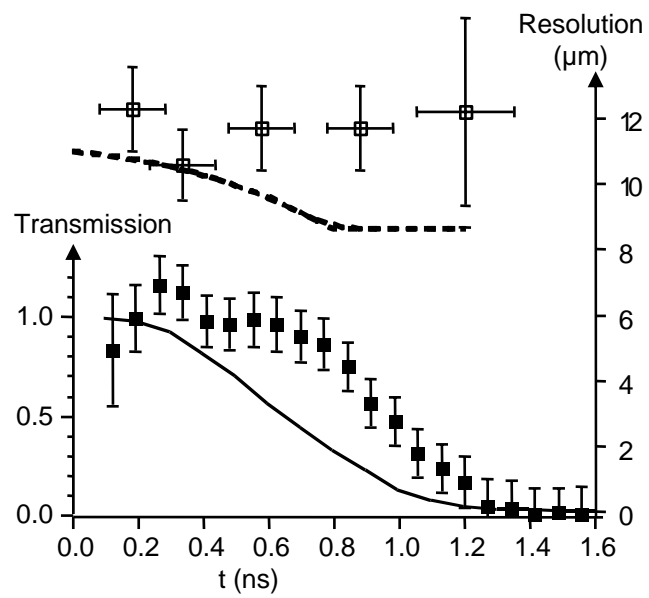


Figure 12

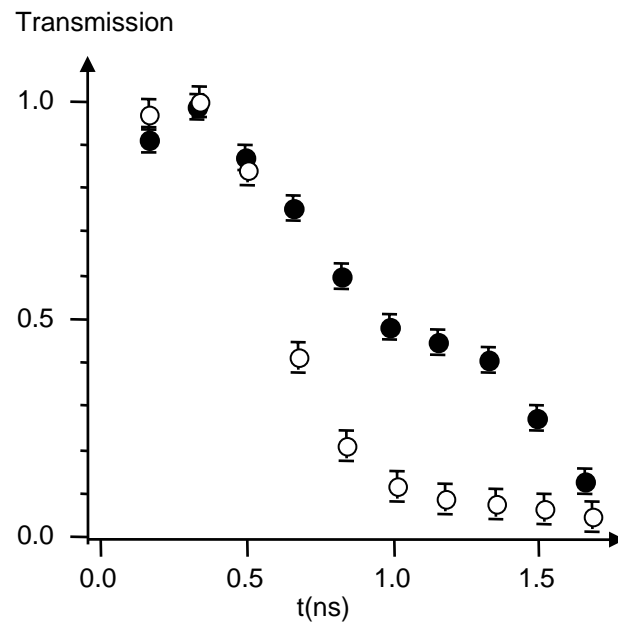


Figure 13